Noname manuscript No.

(will be inserted by the editor)

- Surface Thermal Heterogeneities and The
- 2 Atmospheric Boundary Layer: the Thermal
- 3 Heterogeneity Parameter
- 4 Fabien Margairaz* · Eric R. Pardyjak ·
- 5 Marc Calaf

7 Received: DD Month YEAR / Accepted: DD Month YEAR

Abstract Representing land-atmosphere exchange processes at the ground surface of numerical-weather-prediction models remains a challenge in spite of the recent advances in computing. Previous studies investigating the effects of 10 spatial surface heterogeneities have been viewed from a turbulence perspective, mostly assuming the existence of a blending length scale above which 12 surface-induced perturbations are modelled using an ad-hoc bulk surface pa-13 rameter representing a pseudo-equivalent surface condition. While these types 14 of approaches can generate reasonable results, they fail to account for the long-15 16 lasting spatial perturbations that modify the mean flow. In this work, the interactions between the characteristic scales of surface thermal heterogeneities 17 and the mean resolved fluid dynamics are investigated for a broad range of 18 unstable atmospheric conditions. Thermal dispersive fluxes, which naturally appear as a means to account for persistent-in-time advection fluxes generated 20 by unresolved spatial heterogeneities, provide a quantification of the interac-21 tion between surface thermal heterogeneities and the atmospheric boundary 22 layer mean flow. Hence, they also provide a deterministic approach for including the affect of unresolved processes on the mean flow. We introduce a new 24 nondimensional number (ie, the heterogeneity parameter) that can be used to 25 identify the flow conditions and surface configurations in which heterogeneity effects become important. The heterogeneity parameter can be used to distinguish cases with high and low dispersive-flux contributions based on the mean

Fabien Margairaz

Department of Mechanical Engineering, University of Utah, Salt Lake City, Utah, USA E-mail: fabien.margairaz@alumni.epfl.ch

Eric R. Pardyjak

Department of Mechanical Engineering, University of Utah, Salt Lake City, Utah, USA

Marc Calaf

Department of Mechanical Engineering, University of Utah, Salt Lake City, Utah, USA E-mail: marc.calaf@utah.edu

flow and characteristics of the thermal heterogeneities. These results suggest that under weak geostrophic forcing, surface heterogeneity effects should be accounted for in numerical weather prediction models.

32 Keywords Convective boundary layer, Dispersive flux, Heterogeneity,

³³ Large-eddy simulation, Sensible heat flux

1 Introduction

45

46

47

48

49

50

51

52

53

54

55

56

57

58

59

60

61

62

63

66

67

Land-surface thermal heterogeneities are ubiquitous in nature, and their affect on atmospheric flows is neglected, or at best, coarsely parametrized in numerical weather prediction (NWP) models by more or less accurate correc-37 tions to the traditional Monin-Obukhov similarity-based atmospheric surface 38 layer (ASL) parametrizations. While under certain atmospheric forcing condi-39 tions, such as strong geostrophic forcing, it has been shown that perturbations 40 induced by surface thermal heterogeneities are quickly blended and have neg-41 ligible impact on the flow, in other instances the effect of surface thermal 42 heterogeneities should be considered and hence properly represented in NWP 43 models. 44

If one assumes that the characteristic or dominant length scale of surface thermal heterogeneities (l_h) is larger than the resolution of a NWP model, the corresponding effect of these heterogeneities is resolved and hence accounted for in the model. In this case, the length scale of the mean vertical dynamics (l_d) induced by the thermal patchiness is either much smaller than the surface heterogeneities $(l_d \ll l_h)$ and hence the induced mean vertical motions are easily blended, or are of the same order of magnitude or larger than the surface heterogeneities $(l_d \geq l_h)$ and actively interact with the mean atmospheric boundary layer (ABL) flow. However, since these are larger than the resolution of the NWP model, they require no additional parametrizations.

Alternatively, if one assumes that the characteristic length scale of the surface thermal heterogeneities (l_h) is smaller than the resolution of a NWP model, the corresponding effect of these heterogeneities needs to be parametrized if the mean vertical dynamics (l_d) induced by these thermal patches affects the resolved mean ABL flow. These mean vertical dynamics (herein characterized by l_d) have also been referred to in the literature as turbulence organized structures (TOSs) (Kanda et al. 2004) or thermally-induced mesoscale circulations (TMCs) (Inagaki et al. 2006). An illustration of this conceptual framework linking mean vertically-induced motions, surface thermal heterogeneities, and NWP model resolution is shown in Fig. 1. The aim of this work is to generate new understanding of the interaction between surface thermal heterogeneities and the near-surface ABL flow under a broad range of unstable atmospheric conditions. Therefore, the conceptual hypothesis presented in Fig. 1 is evaluated using the results obtained in this study. Specifically, we are interested in understanding the interaction between surface thermal heterogeneities at unresolved scales in current and near-future

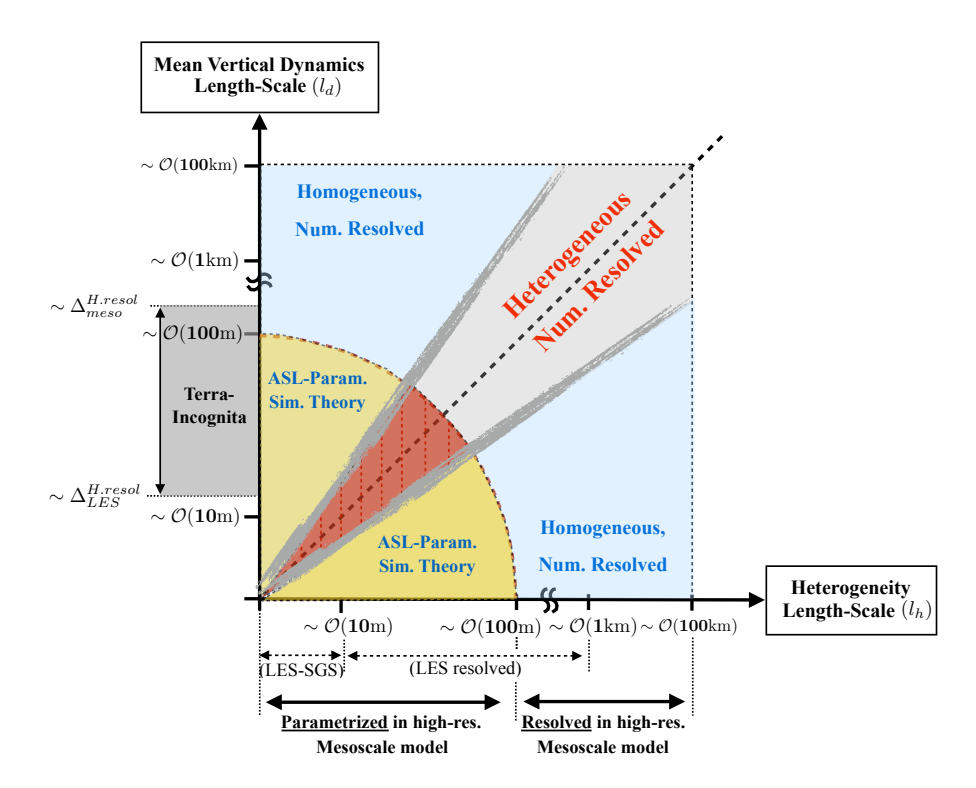


Fig. 1 Illustration of the interaction between mean vertically-induced motions and heterogeneous surface patches of different scales to motivate the need for new ASL parametrisations in mesoscale modeling. (This figure is reproduced here with permission of Boundary-Layer Meteorology, and it was first published in Margairaz et al. (2020))

NWP models and the associated mean vertical motions that can actively disrupt the mean flow. While surface thermal heterogeneities are multiscale in nature, herein we focus the analysis on single-scale heterogeneities, which are representative of the dominant surface-patchiness scale.

This work builds upon the recent analysis of Margairaz et al. (2020), where the possibility of capturing the effects of the unresolved thermal heterogeneities by means of thermal dispersive fluxes (TDFs) was investigated. In this previous work, we presented an LES study of the influence of surface thermal heterogeneities on ABL flows as a function of geostrophic forcing and thermal heterogeneity size. For the first time, we proposed using TDFs as a measure of the impact that surface thermal heterogeneities have on the flow. The results illustrate that under weak geostrophic forcing, TDFs can account for up to 40% of the total sensible heat flux at about $0.1z_i$, with a value of 5-10% near the surface (where z_i represents the ABL height). The term TDF refers to the flux contribution induced by the correlation of the spatial variations of temporal/ensemble-averaged quantities, which differs from the definition of Raupach and Shaw (1982) where discontinuities to spatial derivatives are

introduced by solid boundaries (e.g. vegetated canopies). A similar formulation for the contribution of the time- and space-averaged fluxes was used in Kanda et al. (2004), Inagaki et al. (2006), Mauder et al. (2008), and Zhou et al. (2018) to try to explain the surface energy balance closure problem, where it was found that part of the imbalance was due to heat transport by mean vertical motions. Nonetheless, in Mauder et al. (2008) the actual contribution of the TDFs was neglected, being considered much smaller than the other terms involved in the energy imbalance analysis. Patton et al. (2005) conducted an important large-eddy simulation (LES) study using a similar approach, although spatial averaging was only done in the spanwise direction.

In this work, we investigate the reasons for the existence of TDFs based on the structure of the ABL and thermal forcing conditions. We evaluate the potential for using TDFs to represent the effects of unresolved surface thermal heterogeneities on the mean flow. In addition, we introduce a new nondimensional parameter that defines a threshold beyond which the effects of heterogeneity are significant and the TDFs are relevant. This parameter is intrinsically related to the morphology of the surface thermal heterogeneities and the near-surface mean flow.

In Sect. 2, a derivation of the new non-dimensional parameter is introduced. In Sect. 3 the numerical platform used and study cases are presented. Section 4 relates the structure of the mean ABL flow to the TDF contributions and the new non-dimensional parameter. Finally, a discussion of the results and implications for ASL parametrizations is provided in Sect. 5, with conclusions in Sect. 6.

2 Theory

91

93

94

95

101

102

103

104

105

106

107

108

109

110

111

112

113

116

117

118

119

120

121

123

124

When interpreting the forcing induced by surface thermal heterogeneities on the mean ABL flow, it is helpful to refer to the schematic illustration presented in Fig. 2. As illustrated, the thermal heterogeneities induce a mean vertical flow with a characteristic length scale (l_d) that can either be of similar order (a), much smaller (b), or larger (c) than the heterogeneity scale (l_h) . The flow will be affected by the thermal patchiness via active interactions between buoyancy-induced forcing by surface thermal heterogeneities and the mean horizontal forcing that tends to blend buoyancy effects.

Mathematically, the distinction between the different behaviours should be at least partially prescribed by the mean vertical momentum equation without the viscous term because we are solely interested in high Reynolds number ABL flows. At steady state and over flat terrain, this equation is given by

$$\overline{u}_{j}\frac{\partial \overline{w}}{\partial x_{j}} = -g\frac{\Delta T}{\overline{T}} - \frac{1}{\rho}\frac{\partial \overline{p}}{\partial z} - \frac{\partial}{\partial x_{j}}\overline{u'_{j}w'},\tag{1}$$

where the primes indicate <u>turbulent</u> fluctuations with respect to the time or ensemble averages. Hence, $\overline{u'_jw'}$ represents the traditional turbulent Reynolds shear stress. In the presence of planar homogeneity, a balance between mean

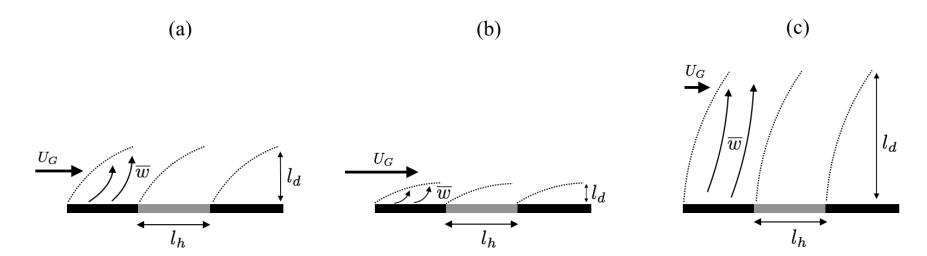


Fig. 2 Schematic illustrating the conceptual interpretation of the interaction between surface thermal heterogeneities and the mean ABL flow. l_h and l_d correspond to the length scales introduced in Fig. 1

pressure gradient and turbulent stress gradient must be maintained (i.e. dominant balance) as indicated in Tennekes and Lumley (1972). Alternatively, in the presence of externally-imposed surface thermal spatial gradients, the 'first responders' are the mean advection terms. Our LES data show that vertical advection dominates horizontal advection for strong convective conditions, while these terms have similar orders of magnitude in strong geostrophic driven flows. Hence, to a first-order approximation, it is fair to rewrite the momentum equation for the mean vertical velocity as a balance between the surface-driven thermal buoyancy and the mean vertical advection,

$$\overline{w}\frac{\partial \overline{w}}{\partial z} = -g\frac{\Delta T}{\overline{T}}.$$
 (2)

From the conservation of mass equation, we can estimate the mean vertical-velocity scale, w^{\dagger} . We assume that the mean horizontal velocity scales as U_G and the length scale of the surface thermal heterogeneities l_h may be taken as a measure of the distance over which the mean vertical velocity will change. Hence, the mean vertical-velocity scale is given by $w^{\dagger} \sim U_G l_d/l_h$. Here, l_d is the characteristic length scale for the vertical flow dynamics. Therefore, the scale analysis yields

$$w^{\dagger} \frac{w^{\dagger}}{l_d} \sim -g \frac{\Delta T}{\overline{T}} \implies \frac{U_G^2 l_d}{l_b^2} \sim g \frac{\Delta T}{\overline{T}}.$$
 (3)

This equation can be further manipulated and expressed as the balance between two non-dimensional terms,

$$\frac{l_d}{l_h} \sim \frac{g \, l_h}{U_G^2} \frac{\Delta T}{\overline{T}} \equiv \mathcal{H},\tag{4}$$

where the right-hand side is hereafter referred to as the thermal heterogeneity parameter and indicated by \mathcal{H} , which represents a ratio of buoyancy to inertial forces. In this equation, we have decided to approximate ΔT as the mean absolute difference between the surface temperature at a point and the overall averaged surface temperature, $\langle |T_s - \langle T_s \rangle| \rangle$. Therefore, one can physically interpret the buoyancy term as the potential vertical momentum a mass

of air could have if it remained in the vicinity of the surface thermal heterogeneity. While this remains a conceptual interpretation, it is enough to provide a physical bound to the mean vertical momentum induced by the surface heterogeneities. In contrast to the traditional mean vertical momentum balance where the buoyancy term is based on air temperature, the relative surface temperature ($\Delta T/\bar{T}$) used here can be considered as an upper limit on the buoyancy term, where turbulence is blending the surface temperature differences and reducing it in the air.

The heterogeneity parameter can also be rewritten as the product of two terms: an inverse squared Froude number $(F_r^{-2} = gl_h/U_G^2)$ and a relative measure of the surface-temperature heterogeneity $(\Delta T/\overline{T})$. This derivation treats the heating and cooling of the surface as the driving force that generates temperature perturbations in the flow field where the amplitude is dependent on the surface-temperature heterogeneity. From the balance indicated in Eq. (4), it can be further observed that when $\mathcal{H} \gg 1$ then $l_d \gg l_h$, and hence the surface heterogeneities induce strong perturbations on the mean flow. Alternatively, when $\mathcal{H} \ll 1$, the characteristic length scale of the heterogeneities is larger than that of the induced vertical dynamics $(l_h \gg l_d)$, hence facilitating blending of the surface-induced thermal perturbations.

As will be presented later on, this parameter plays an important role in determining when surface thermal heterogeneities actively interact with the mean ABL flow.

3 Methodology and Study Cases

The different ABL flows used in this work are modelled using the pseudo-spectral LES approach introduced by Moeng (1984) and Albertson and Parlange (1999), later modified by Bou-Zeid et al. (2005), Calaf et al. (2011), and Margairaz et al. (2018). This framework is based on the non-dimensional, filtered, incompressible Navier–Stokes equations, coupled with a filtered temperature transport equation. Details of the numerical approach can be found in the Appendix.

In order to study the effects of surface thermal heterogeneities, two types of simulations are considered. The first type uses a homogeneous surface temperature of 290 K. This first type acts as a control group. In the second type, a patchy surface temperature distribution is obtained using a Gaussian distribution with a mean temperature of 290 K and a standard deviation of 5 K. Three different square patch sizes of 800, 400, and 200 m are considered, as shown in Fig. 3. Additionally, to ensure that the results are not dependent on patch distribution, three extra distributions are implemented for the 800-m size patches. The results presented in Margairaz et al. (2020) showed little dependence on patch distribution, and hence in this work, only one 800-m patch configuration is analyzed in detail. Similarly, those results showed that, for the purpose of this study, the outcome did not change significantly when considering a domain twice the size of the current configuration.

196

197

198

200

201

202

203

204

205

206

207

208

209

210

211

213

214

215

216

217

218

219

220

221

223

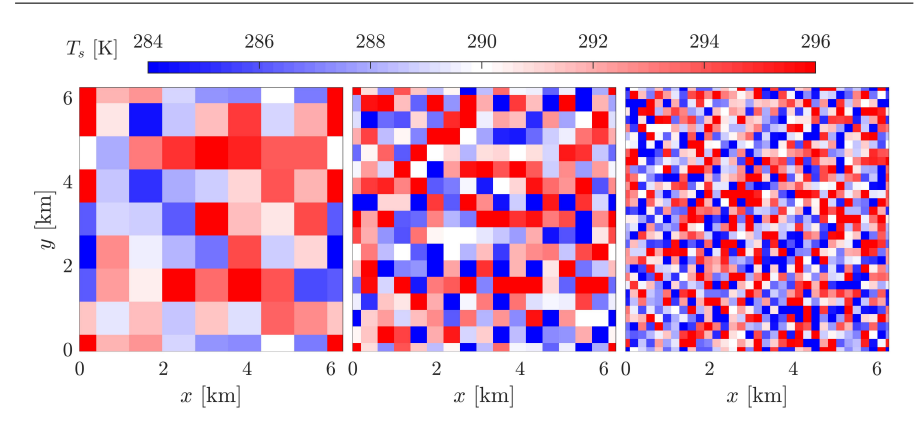


Fig. 3 Surface temperature distributions for the cases with heterogeneous patches. From left to right: 800-m patches (HT-X-s800), 400-m patches (HT-X-s400), and 200-m patches (HT-X-s200)

The bottom boundary condition uses Monin-Obukhov similarity theory to obtain the surface heat flux from the surface temperature, which is kept constant throughout the simulations. Hence, there is no feedback from the atmosphere to the surface as the surface does not cool down or warm up with local changes in velocities. In addition, the ABL gradually warms as the simulations are running, resulting in it becoming less convective overtime. However, the runs are not long enough for this to be significant. In all cases, the surface roughness is set to 0.1 m (representative of a surface with sparse forest or farmland with many hedges (Brutsaert 1982; Stull 1988)) and the initial boundary-layer height is set to $z_i = 1000$ m. The temperature profile is initialized with a mean air temperature of 285 K and a capping inversion of Γ = 0.012 K m⁻¹ is prescribed at z_i . For each surface condition, a wide range of geostrophic wind speeds is considered $(U_g = 1, 2, 3, 4, 6, 9, 15 \text{ m s}^{-1})$. The flow is driven with a constant pressure gradient obtained through the geostrophic approximation, which accounts for the Coriolis force due to rotation of the Earth. The Coriolis parameter is set to $f_G = 10^{-4}$ Hz, corresponding to a latitude of 43.3° N.

Throughout this work, the homogeneous cases are referred to as HM-X where X indicates the corresponding geostrophic wind speed. Similarly, the heterogeneous cases are denoted as HT-X-sYYY, where X indicates the corresponding geostrophic wind speed and sYYY refers to the size of the patches (e.g. HT-1-s200 would be the heterogeneous case with 200-m patches, and forced with $U_g = 1 \text{ m s}^{-1}$). In total, 28 different configurations have been considered for this study. A detailed overview of the study cases is given in Table 1.

In all cases, a numerical domain of $(L_x, L_y, L_z) = (2\pi, 2\pi, 2)$ km is used with a grid size of $(N_x, N_y, N_z) = (256, 256, 256)$ yielding a horizontal resolution of $\Delta x = \Delta y = 24.5$ m and a vertical grid spacing of $\Delta z = 7.8$ m. The timestep is set at $\Delta t = 0.1$ s to ensure the stability of the time integration.

Table 1 Summary of the study cases and the corresponding most relevant 30-min average simulation statistics. The properties presented in the table are the geostrophic forcing velocity (U_g) , the boundary-layer height (z_i) , the Obukhov length $(L=-(u_*^3\theta_S)/(\kappa g\overline{(w'\theta')_S}))$, the stability parameter $(-z_i/L)$, the friction velocity (u_*) , and the Deardorff convective velocity scale $(w_*=(gz_i\overline{(w'\theta')_S}/\bar{\theta}_S)^{1/3})$. The boundary-layer height and the Obukhov length have been rounded up to the nearest m. The stability factor has been rounded up to the nearest integer

Name	U_{a}	z_i	L	$-z_i/L$	u_*	w_*
	$_{\mathrm{m\ s}^{-1}}^{U_{g}}$	m	m	-	${ m m~s^{-1}}$	${ m m~s^{-1}}$
HM-1	1	1328	-4	315	0.17	1.31
HM-2	2	1318	-6	205	0.20	1.30
HM-3	3	1306	-12	113	0.24	1.30
HM-4	4	1293	-19	68	0.28	1.30
$_{HM-6}$	6	1295	-44	30	0.37	1.30
HM-9	9	1307	-95	14	0.49	1.32
HM-15	15	1340	-259	5	0.70	1.35
HT-1-s800	1	1487	-1	3361	0.09	1.47
HT-2-s800	2	1459	-2	883	0.15	1.51
HT-3-s800	3	1448	-5	318	0.21	1.51
HT-4-s800	4	1431	-9	157	0.26	1.49
HT-6-s800	6	1397	-23	61	0.35	1.48
HT-9-s800	9	1394	-64	22	0.48	1.46
HT-15-s800	15	1407	-194	7	0.70	1.47
HT-1-s400	1	1487	-1	3433	0.10	1.51
HT-2-s400	2	1463	-2	897	0.15	1.55
HT-3-s400	3	1452	-4	397	0.20	1.54
HT-4-s400	4	1434	-8	170	0.26	1.52
HT-6-s400	6	1406	-22	63	0.35	1.50
HT-9-s400	9	1390	-62	22	0.48	1.47
HT-15-s400	15	1404	-197	7	0.70	1.46
HT-1-s200	1	1439	-1	1741	0.12	1.53
HT-2-s200	2	1434	-2	933	0.15	1.53
HT-3-s200	3	1430	-4	377	0.20	1.54
HT-4-s200	4	1434	-8	180	0.25	1.53
HT-6-s200	6	1402	-23	61	0.35	1.50
HT-9-s200	9	1374	-65	21	0.48	1.46
HT-15-s200	15	1383	-207	7	0.70	1.44

Converged turbulence statistics are obtained for a period of one hour after a spin-up period of 4 hours. This period corresponds to ≈ 2.3 turnover times $(T = U_g t/L_x)$ for the weakest geostrophic forcing case: $U_g = 1 \text{ m s}^{-1}$. During the evaluation phase, statistics are computed for averaging times ranging between five minutes and one hour. Statistical convergence is achieved using 30-min averages. Negligible changes are observed with 60-min averages. More details on the study cases are included in Margairaz et al. (2020).

²³¹ 4 Structure of the Atmospheric Boundary-Layer Flow

In this section, the results are presented in three parts: the first part discusses
the effect of surface heterogeneities on the turbulent flow, the second part
focuses on the time-averaged flow field, and the third part explains the role of
TDFs.

4.1 Turbulent Flow

237

239

240

242

244

245

246

248

249

250

251

252

253

254

255

256

257

259

260

261

263

264

265

267

268

269

271

To qualitatively help understanding the effect of surface thermal heterogeneities on the turbulent ABL flow, we first present the vertical velocity fluctuations. Figure 4 shows isosurfaces of the vertical velocity fluctuations between the ground surface and a height of $z/z_i=0.5$ for the different surface conditions and two different geostrophic wind speeds. The isosurfaces of $w'/w_*=\pm 1$ encapsulate the regions of upward and downward motion.

In the case of $U_g=1~\mathrm{m~s^{-1}}$ over a homogeneous surface, the flow corresponds to the well-documented case of cell-type free convection (Konrad 1970; Weckwerth et al. 1999; Bennett et al. 2010; Salesky et al. 2017). Large open cells of upward motion, whose sizes can vary from $\approx 2-4$ km, surround regions of downward motion. Within these open cells, small upward plumes of $\approx 200-400$ m are also present. Most of the structures are vertically aligned due to the low shear produced by the weak geostrophic forcing. In contrast, when the geostrophic forcing is strong (e.g. $U_g = 15 \text{ m s}^{-1}$), the flow has a completely different structure. In this case, the convective motions are modified and take on a roll-type character. The open cells observed previously have been destroyed by the strong wind forcing, and large, elongated structures are now observed. These large structures of upward motion are aligned with the mean wind direction and are tilted as a consequence of the high shear due to the strong forcing. These elongated streaks are several kilometers long and are separated by regions of downward motion. In the same figure, the effect of surface heterogeneities on the cell-type structures can be observed in the left panel. The presence of colder patches degrades the well-structured convective motions, with a partial or complete lack of vertical motion above them. The larger patches (800 m) have a significant effect on the cell structure where a complete lack of well-organized large open cells can be observed. In contrast, the small patches (200 m) seem to prevent the formation of wellorganized, large open cells like the ones formed above the homogeneous surface. In this case some disordered cell type of large-scale structures of upward motion are instead observed. In addition, some small plumes of upward motion of $\approx 200-400$ m form above the hotter patches. The interaction between the different length scales of the patches and the length scales found in cell-type convection is described in more detail in Margairaz et al. (2020). Alternatively, under the strong wind conditions, the surface thermal heterogeneities do not seem to have a significant effect on the roll-type flow structure. The cold

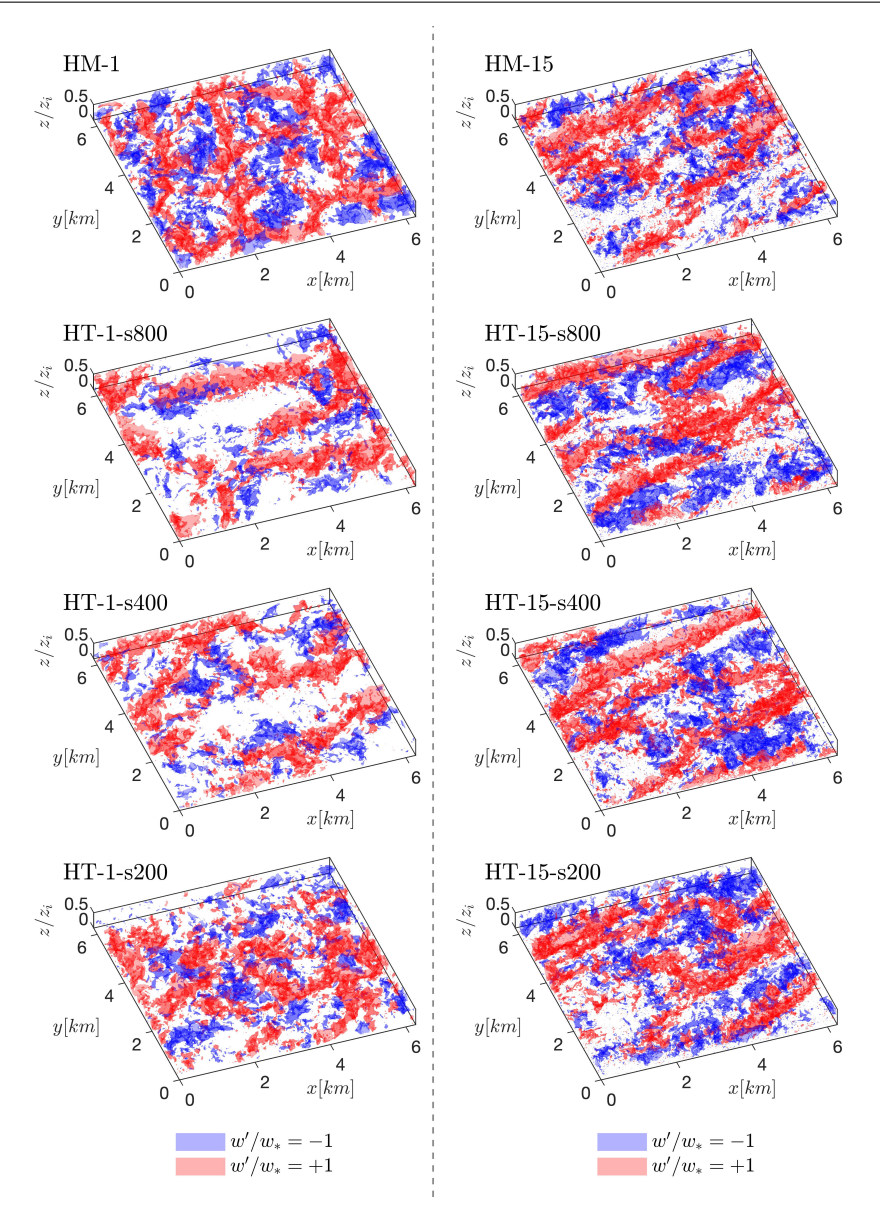


Fig. 4 Isosurfaces of the vertical velocity fluctuations in the lower half of the boundary layer $(0 \le z/z_i \le 0.5)$. The positive fluctuations of w'/w*=+1 are shown in red and the negative fluctuations of w'/w*=-1 are shown in blue

patches do not affect the convective motion because the high shear produced by the strong geostrophic forcing blends them.

272

273

275

The transition between cell- and roll-type convection can be quantified using the roll factor metric developed by Salesky et al. (2017). This method is

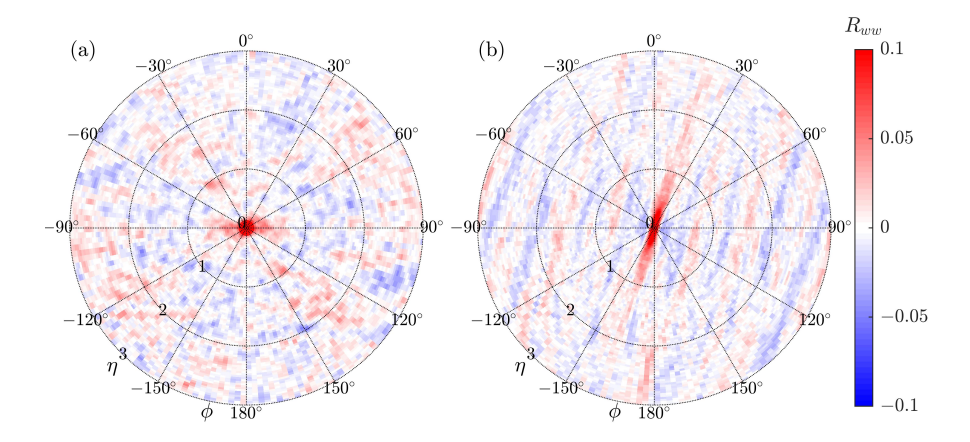


Fig. 5 Two-point correlation function of the vertical velocity $R_{w\,w}$ for (a) HT-1-s800 and (b) HT-15-s800 cases at $z/z_i\approx 0.025$ m above the ground

based on the two-point correlation function of the vertical velocity in cylindrical coordinates $R_{ww}(r_{\eta}, r_{\phi}, z)$ where r_{η} is the radial lag, r_{ϕ} is the angular lag, and z is the height above the ground. Figure 5 shows the two-point correlation function for the HT-1-s800 and HT-15-s800 cases at 32 m above the ground. This height corresponds to the fourth vertical grid point in the LES, and hence the effects of the wall model are mostly diffused. Additionally, this height corresponds to the first grid point of most NWP models. These two cases exemplify the differences that are observed between the weak and strong geostrophic forcing cases. In the left panel, the center correlation exhibits an axisymmetric character, indicative of a cell-like structure in the flow. Also, circular spots of positive and negative correlation are randomly distributed around the center. This behaviour is characteristic of cell-type convection. In contrast, the strong geostrophic case exhibits elongated zones of high correlation, indicating that the flow is organized in long and streak-like structures. This is typical of roll-type convection.

The method developed in Salesky et al. (2017) facilitates detecting the angular dependencies of the roll-type convection using the statistical range of the two-point correlation function. The range, defined as

$$R(r_{\eta}) = \max_{r_{\phi}} \left[R_{ww}(r_{\eta}, r_{\phi}, z) \right] - \min_{r_{\phi}} \left[R_{ww}(r_{\eta}, r_{\phi}, z) \right], \tag{5}$$

takes on large values for roll-type convection as R_{ww} goes from positive to negative values over a circle of a given radius around the origin. In contrast, the statistical range does not vary much in the case of cell-type convection. The maximum value over all radii is called the roll factor and is defined as

$$\mathcal{R} = \max_{r_{\eta}} \left[R(r_{\eta}) \mid r_{\eta}/z_{i} \ge 0.2 \right]. \tag{6}$$

Following this definition, a large roll factor corresponds to roll-type convection and a small roll factor to cell-type convection. In order to only characterize

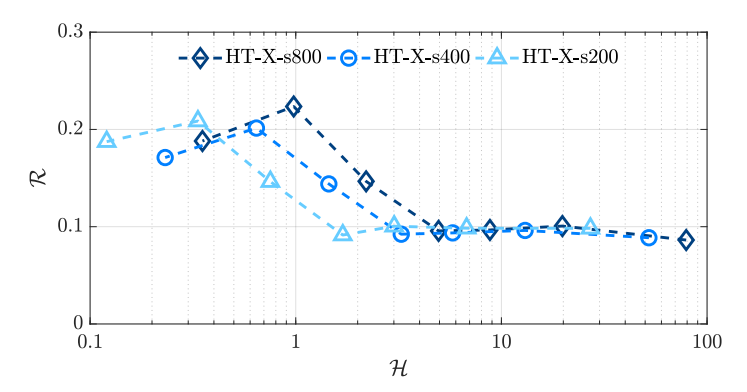


Fig. 6 Roll factor \mathcal{R} as a function of the heterogeneity parameter \mathcal{H} at $z/z_i \approx 0.025$

large-scale coherent motions and to avoid minor fluctuations of the two-point correlation function close to the origin $(r_{\eta}/z_i=0)$, it is necessary to limit the analysis to large radial lags. The value of this cut-off needs to be adjusted as the size of the coherent structure increases with height. At $z/z_i\approx 0.025$, the radial lag cut-off is set to $r_{\eta}/z_i\geq 0.2$.

Using this metric, the cases with homogeneous surface conditions match the results presented by Salesky et al. (2017) with $\mathcal{R} \sim 0.1$ for weak forcing $(U_g=1~\mathrm{m~s^{-1}}, -z_i/L=315)$ computed at $z/z_i=0.5$ using a radial lag cutoff of $r_\eta/z_i \geq 0.5$. Similarly, for the case with strong forcing $(U_g=15~\mathrm{m~s^{-1}}, -z_i/L=5)$, a value of $\mathcal{R} \sim 0.3$ is observed. The transition between the modes of convection occurs between $U_g=4~\mathrm{m~s^{-1}}$ and $U_g=6~\mathrm{m~s^{-1}}~(-z_i/L\approx120~\mathrm{mod}~z_i/L\approx30)$. Similarly, for the heterogeneous surface conditions, the transition between cell- and roll-type convection occurs between $U_g=4~\mathrm{m~s^{-1}}$ and $U_g=9~\mathrm{m~s^{-1}}~(-z_i/L\approx180~\mathrm{mod}~z_i/L\approx20)$ with small variations between the cases.

Figure 6 shows the roll factor \mathcal{R} as a function of the heterogeneity parameter \mathcal{H} introduced in Sect. 2. The roll factors obtained for the different surface distributions and wind forcings collapse the data quite well, indicative of the appropriateness of the new non-dimensional parameter. The results indicate the existence of three different regimes. The first regime, $\mathcal{H} \lesssim 1$ and $\mathcal{R} \gtrsim 0.1$, corresponds to roll-type convection indicative of a flow dominated by shear. The second regime, $1 < \mathcal{H} < 5$, corresponds to a transition zone in which both thermal heterogeneity and mean wind shear are in strong competition. Finally, the third regime is characterized by $\mathcal{H} > 5$ and $\mathcal{R} \sim 0.05$, corresponding to cell-type convection of a flow dominated by buoyancy forcing. It is important to note that the homogeneous case is an ill-defined limit of the heterogeneity parameter. Therefore, the roll factor obtained for the homogeneous case cannot be represented in Fig. 6.

The height $z/z_i \approx 0.025$ has been selected for this analysis because it roughly corresponds to the lowest grid point in NWP models. This height is

particularly important since the effects of subgrid-scale heterogeneities will need to be parameterised in the models at this level.

4.2 Mean Flow

In this section, we quantify some of the effects of surface thermal heterogeneities on the mean vertical velocity field. Fig. 7 shows isosurfaces that correspond to plus/minus one standard deviation of the time-averaged vertical velocity, which represent regions dominated by either upward or downward vertical motion. The figure illustrates that for weak geostrophic wind speeds, the mean footprint of the cell-type convection is preserved.

It is particularly interesting to identify the differences observed in the heterogeneous surface cases, where the patchiness strongly affects the mean vertical velocity field. Specifically, note that regions with dominant upward motions are mostly located above the hot patches, and the regions of dominant downward motion are found predominantly above the cold patches. Alternatively, for those cases with strong geostrophic forcing (e.g., $U_g=15~{\rm m~s^{-1}}$), the time-averaged vertical velocity exhibits a completely different structure, with almost no difference between the homogeneous and heterogeneous surface cases. Also, the number of rolls present in the domain appears to be almost unchanged, indicative that these are mostly result of the shear stress, and are only weakly influenced by the thermal heterogeneity. Hence, under strong wind conditions, the effect of the surface heterogeneity is clearly blended.

To objectively quantify these differences, we interrogate the corresponding probability distribution functions (p.d.f.s) of the mean vertical velocity, with a detailed quantification of the mode, skewness, and kurtosis. This is represented in Fig. 8, which indicates that all homogeneous cases (red lines) yield a distribution nearly centered around $\bar{w}/w_* = 0$ and are slightly positively skewed. In addition, the distribution becomes narrower and more peaked with increasing geostrophic forcing. This indicates that the number of upward time-persistent motions is slightly greater than the number of downward time-persistent motions. In contrast, the distribution for the heterogeneous cases is more positively skewed, with a longer positive velocity tail. Hence, the heterogeneous surface conditions tend to yield more negative velocity occurrences, with fewer but stronger time-persistent upward motions. This observation matches well with earlier results of Patton et al. (2005). As the geostrophic forcing increases, the p.d.f.s of the heterogeneous cases become more and more similar to those obtained for the homogeneous cases, as expected. This is illustrated in the mean flow field in Fig. 7. In these stronger wind conditions, the p.d.f.s become narrower and the modes of the p.d.f.s become closer to $\bar{w}/w_* = 0$.

Fig. 9 presents the corresponding moments of the p.d.f.s as a function of the heterogeneity parameter (\mathcal{H}) , illustrating once again a clear relationship. In Fig. 9a, it can be observed how the corresponding modes become close to 0 m s⁻¹ when $\mathcal{H} < 1$, and greater than zero in absolute value for large values of the heterogeneity parameter $(\mathcal{H} > 5)$. Therefore, as subjectively illustrated

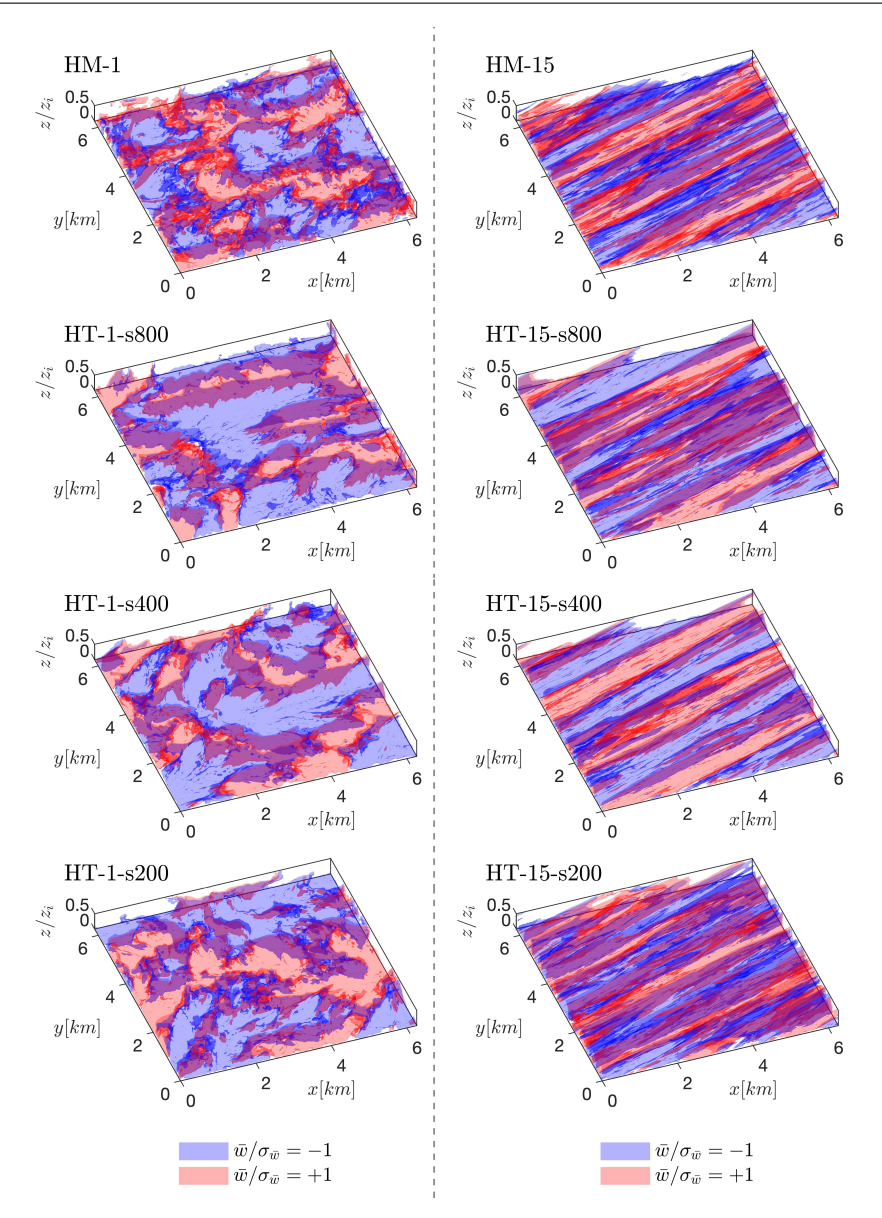


Fig. 7 Isosurfaces of the 30-min time-averaged vertical velocity in the lower half of the boundary layer ($0 \le z/z_i \le 0.5$). The isosurfaces correspond to vertical velocity of $\bar{w} = \pm \sigma_{\bar{w}}$ of the 30-min average vertical velocity at a height of $z/z_i \approx 0.025$

before in Fig. 7, when heterogeneity is small, the mean vertical velocity is close to zero, while when heterogeneity is present, a dominant negative mean vertical velocity is induced in the flow field that is only counteracted by isolated and starker positive mean vertical motions. This is further confirmed by the

373

374

375

376

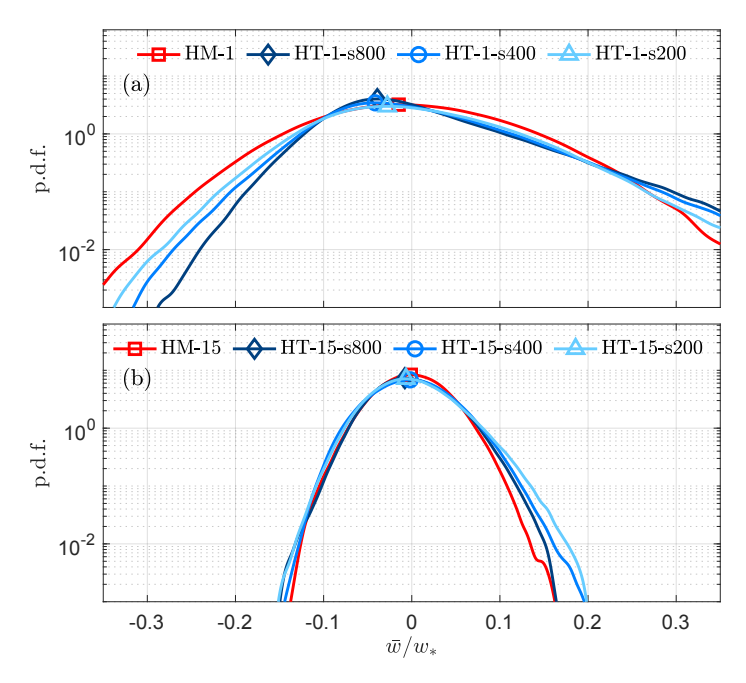


Fig. 8 Probability density function of the time-averaged vertical velocity at $z/z_i \approx 0.025$ for (a) weak geostrophic forcing and (b) strong geostrophic forcing. The marker represent the mode of the p.d.f.s

skewness, presented in Fig. 9b. It shows that the distribution becomes more symmetric (smaller values) with smaller values of the heterogeneity parameter. Figure 9c shows the kurtosis, which represents the relevance of the tails of the distribution. It indicates that the p.d.f.s resemble a quasi-Gaussian distribution with kurtosis values close to 3 for $\mathcal{H} < 1$. In contrast, the kurtosis takes on larger values with increasing heterogeneity $(\mathcal{H} > 5)$.

In summary, the different moments of the p.d.f.s confirm that for small heterogeneity parameters ($\mathcal{H}<1$), the distribution tends to be similar to those obtained for the homogeneous cases, while for larger values of the heterogeneity parameter ($\mathcal{H}>5$) the distribution of the mean vertical velocity is changed with the potential to more intensely disrupt the local mean ABL flow. Furthermore, the clear relationship observed with the heterogeneity parameter \mathcal{H} is taken as indicative of its capacity for quantifying the effects of surface thermal heterogeneities, and the corresponding blending.

Note that the moments of the mean vertical velocity represented in Figs. 8 and 9 have been normalized by w_* . Although, the Deardorff convective velocity scale might not be the most appropriate scaling velocity for the time-averaged vertical velocity, the figures describe the structure of the flow and normalization facilitates comparison between cases. Therefore, in lieu of a better normalization, we use w_* .

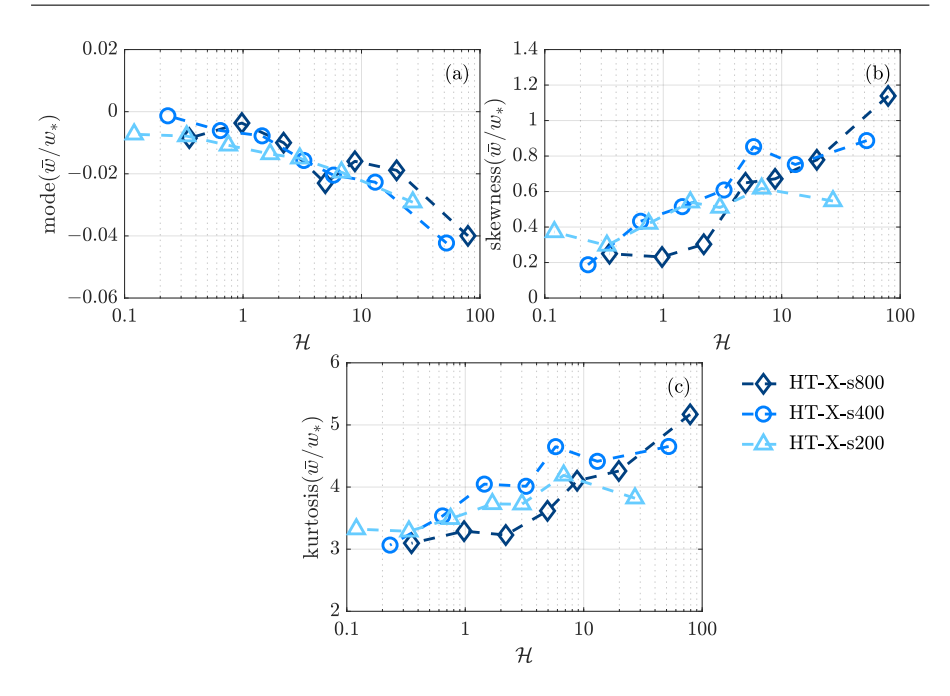


Fig. 9 Moments of the p.d.f.s of the mean time-averaged vertical velocity as function of \mathcal{H} at $z/z_i \approx 0.025$. The panels are: (a) the mode, (b) the skewness, and (c) the kurtosis

4.3 Thermal Dispersive Fluxes

Next, we investigate TDFs and their link to the different regimes observed in previous section. Based on Raupach and Shaw (1982), a TDF is defined as $Q_{disp} = \langle \bar{w}''\bar{T}'' \rangle$, where the time-averaged spatial fluctuation of the vertical velocity is defined as $\bar{w}'' = \bar{w} - \langle \bar{w} \rangle$, \bar{w} is the time averaged vertical velocity, and $\langle \bar{w} \rangle$ is the spatial average of the time-averaged vertical velocity. The temperature is decomposed similarly. In this analysis, the TDFs have been computed using the 30-min time-averaged quantities, and using spatial averages of the entire numerical domain (see Margairaz et al. 2020 for more details regarding sensitivity to averaging time).

Hence, the transition between the different regimes characterized by the heterogeneity parameter can be linked to the corresponding contribution of the TDFs. This is illustrated in Fig. 10, where the ratio of the TDFs to the turbulent heat fluxes is presented as a function of the heterogeneity parameter \mathcal{H} at $z/z_i \approx 0.025$. Here, the same previous three regimes can be identified, with an improved collapse of the data with the heterogeneity parameter (\mathcal{H}). In the first regime ($\mathcal{H} < 1$), the contribution of the TDFs is small, $Q_{disp}/Q_{turb} < 0.05$. In the transitional regime, $1 < \mathcal{H} < 5$, the contribution of the TDFs increases to be between $0.05 < Q_{disp}/Q_{turb} < 0.1$. Finally, the third regime ($\mathcal{H} > 5$) exhibits a considerable contribution of the TDFs, $0.1 < Q_{disp}/Q_{turb} < 0.2$. Therefore, results show how large values of the heterogeneity parameter (\mathcal{H})

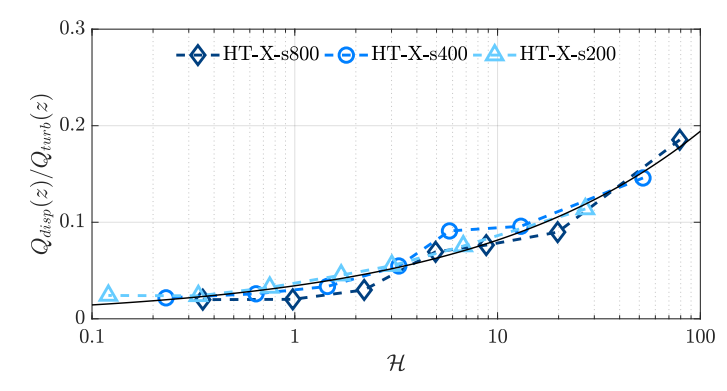


Fig. 10 Ratio of the TDF (Q_{disp}) to the turbulent heat flux Q_{turb} as a function of the heterogeneity parameter \mathcal{H} at $z/z_i \approx 0.025$. The black line represents the power law $Q_{disp}/Q_{turb} = \alpha \mathcal{H}^{\beta}$

are indicative of situations in which the flow and surface configurations can produce a significant TDF contribution, synonymous with strong and persistent thermal patterns. Alternatively, small values of \mathcal{H} indicate that the horizontal mean flow can blend the contribution of the surface patches well enough to prevent a substantial contribution of the TDFs to the heat transport process. In addition, the data fit the power law $Q_{disp}/Q_{turb} = \alpha \mathcal{H}^{\beta}$ well, where the coefficients are $\alpha = 0.0342$ and $\beta = 0.3769$. Hence, the TDF contribution of can be estimated directly from the thermal heterogeneity parameter.

Further, because the heterogeneity parameter (\mathcal{H}) encapsulates both the information about the surface heterogeneities (i.e., size and intensity) as well as the information about the mean flow responsible for the shear, it seems clear that the interaction between the heterogeneity length scale (l_h) and the corresponding induced mean-flow-dynamics length scale (l_d) should be well explained by the heterogeneity parameter (\mathcal{H}) , which is further related to the corresponding contribution of the TDFs. In this regard, given that the heterogeneity parameter can also be written as a function of the Froude number (see Sect. 2), it is possible to define $\mathcal{H} < 1$ as some subcritical regime where the impact of thermal heterogeneities is quickly blended by the airflow, and $\mathcal{H} > 5$ as a supercritical regime where the surface temperature perturbations propagate across the ABL, thus leading to large TDFs.

These observations are summarized in Fig. 11, which evaluates the initial hypothesis presented in Fig. 1 in the context of our LES results. As originally illustrated in the introductory figure, the horizontal and vertical axes represent the interaction between the heterogeneity length scale (l_h) and the corresponding induced mean-flow-dynamics length scale (l_d) . The results for all study cases are shown as coloured circles, where the colour is related to the corresponding relative contribution of the TDFs. The red dashed lines indicate the approximate current resolution in NWP models (1 km), and the black dashed lines illustrate the identified limiting cases of the heterogeneity parameter (i.e. $\mathcal{H} = 1, 2$, and 5). As previously illustrated in Fig. 10, those

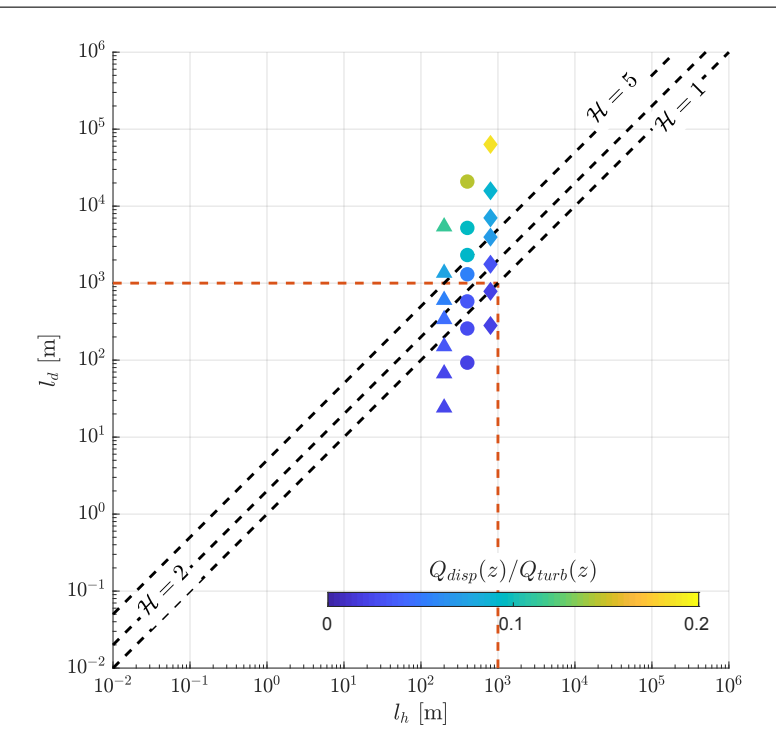


Fig. 11 Interaction between the heterogeneity length scale (l_h) and the mean flow dynamics length scale (l_d) . The shape of the symbols designates the different cases: diamonds represent HT-X-s800, circles correspond to HT-X-s400, and triangles illustrate HT-x-s200. The colour of the symbols represents the ratio for TDF over the turbulent flux measured at $z/z_i \approx 0.025$. The black dashed-lines illustrate the case of $\mathcal H$ where the transitions between regimes are observed

cases with $\mathcal{H} > 5$ have a significant contribution to the TDFs (warmer colour), and hence should be accounted for in NWP models. This is further justified through this figure, not only because of their significant contribution to the overall sensible heat fluxes, but also because these unresolved surface thermal heterogeneities ($l_h < \Delta$, with Δ being the numerical grid resolution) have the potential to generate flow dynamics of a scale larger than the numerical resolution ($l_d > \Delta$). This can be observed through the fact that the warm colour-filled circles reside above the red horizontal dashed line.

In particular, Fig. 11 provides a means to predict what size of surface thermal heterogeneities are required to generate a given dynamical scale, for a specified set of geostrophic forcing and mean surface temperature fluctuations. This is indicated by the diagonal grey lines, where each one represents the relation $l_d = \frac{g}{U_G^2} \frac{\Delta T}{T} l_h^2$. Hence, the slope $(\frac{g}{U_G^2} \frac{\Delta T}{T} l_h)$ illustrates a unique combination of ΔT , T, and U_G for any fixed l_h , which can be interpreted as a potential forcing. Therefore, for a fixed combination of ΔT , T, and U_G (hence any grey-like diagonal line), Fig. 11 allows one to identify the size of surface

thermal heterogeneity (l_h) needed (starting point of the grey line) to generate a mean-flow-dynamic scale l_d larger than the given numerical resolution Δ of interest, and with an $\mathcal{H} \geq 5$.

5 Discussion

468

469

470

472

473

474

475

476

478

479

481

482

483

484

485

486

487

489

490

491

492

493

495

496

497

499

501

502

503

505

The working hypothesis of this study is that land-surface thermal heterogeneities actively interact with the mean atmospheric flow under certain forcing conditions and that this interaction can be accounted for by a representation that includes TDFs. While we analyzed the initial part of this hypothesis in an earlier work (Margairaz et al. 2020), here we focus the analysis on the link between the structure of the ABL flow and the corresponding contributions of the TDFs. Further analysis of TDF contributions is needed for cases when the thermal inertia of the surface is not infinite and the surface is allowed to thermally interact with the ABL flow.

Herein, we proposed a new thermal heterogeneity parameter \mathcal{H} to describe the dynamics induced by thermal heterogeneities. This parameter represents the balance between the effects of surface heterogeneities (through their size l_h and intensity ΔT_s) and mean flow dynamics (characterized by U_q). Moreover, H seems to capture two different regimes observed in the flow well. Namely, small values of \mathcal{H} describe a regime where shear dominates and where the TDFs are small. In this case, the mean vertical velocities follow a Gaussian distribution, similar to the distribution observed above homogeneous surfaces, and the mean horizontal flow is organized in the shape of elongated tubular structures. In this case, the local dynamics of the mean flow do not 'sense' or at least do not obviously respond to the surface thermal heterogeneities. In contrast, large values of $\mathcal{H} > 5$ correspond to instances where heterogeneous surface conditions strongly affect the flow dynamics as a result of weak horizontal wind speeds and strong thermal variations induced by buoyancy. In this case, the mean vertical velocities exhibit a clear departure from the Gaussian distribution as the p.d.f.s become positively skewed, and the contribution of the TDFs is significant.

Despite the success of the heterogeneity parameter in discerning the conditions in which surface heterogeneities affect the mean atmospheric flow, one should not expect this to work equally well to describe the turbulent structure of the flow. This is illustrated in Figure 6 where the collapse of the curves for the roll factor is not perfect, indicative that other scaling variables should be considered.

The results presented here provide a fundamental basis for developing a new framework that can be used to improve the ability of NWP models to capture the effects induced by subgrid-scale thermal heterogeneities. Depending on the heterogeneity parameter, thermal surface heterogeneities may induce resolved-scale effects, and hence, have the potential to significantly alter modelled winds in the ABL.

6 Conclusion

507

508

509

511

512

513

514

515

516

517

519

520

521

522

523

524

525

526

528 529

531

532

533

534

536

537

538

539

540

541

542

545

546

The work presented in this paper builds on a previous study investigating the impact of surface thermal heterogeneities on ABL flow and the importance of the TDFs as a function of geostrophic forcing and thermal-patch size (Margairaz et al. 2020). In this work, we have introduced a new heterogeneity parameter, \mathcal{H} , that describes the dynamics of surface thermal heterogeneities. It represents a balance between the buoyancy effects of surface thermal heterogeneities and inertia of the mean flow. Large values of \mathcal{H} correspond to situations where heterogeneous surface conditions dominate the flow dynamics and where TDFs are important. In contrast, small values of \mathcal{H} describe a regime where shear dominates and TDFs are negligible. It is important to note that this study and the development of the heterogeneity parameter were achieved with a one-way coupling of the surface with the flow (i.e. with an infinite thermal inertia of the surface). Further investigations of the heterogeneity parameter are needed when the surface is allowed to thermally interact with the ABL flow.

Acknowledgements The authors would like to thank Prof. Katul (Duke University) for fruitful discussions. This project has been developed with the support of the U.S. National Science Foundation grant number PDM-1649067. Marc Calaf also acknowledges the Mechanical Engineering Department at the University of Utah for start-up funds, and the Center for High Computing Performance (CHPC) at the University of Utah for computing hours. This work used the Extreme Science and Engineering Discovery Environment (XSEDE), which is supported by National Science Foundation grant number ACI-1548562. The authors declare no conflict of interest.

530 Appendix: Large-Eddy Simulations Framework

The different ABL flows used in this work are modelled with an LES framework where the non-dimensional, filtered, incompressible Navier-Stokes equations are solved using a pseudo-spectral approach (Moeng 1984; Albertson and Parlange 1999). In this framework, the rotational form of the momentum equations is used to ensure conservation of mass and energy in the inertial terms (Kravchenko and Moin 1997). The filtered potential temperature is modelled with an advection-diffusion equation. The Buoyancy forces are computed with the Boussinesq approximation to couple the temperature to the momentum equation (Tritton 1988). This method makes it possible to account for the fluctuations of density through the fluctuations of the temperature field. The sub-grid scale stresses and heat fluxes are computed using the Lagrangian scale-dependent dynamic Smagorinsky models for momentum and scalars (Bou-Zeid et al. 2005; Calaf et al. 2011). The viscous and molecular diffusive effects can be neglected because of the high Reynolds number of the ABL flow. The active Coriolis effects drive the flow through the pressure gradient induced by the geostrophic forcing. To integrate the equations in time, the Chorins projection fractional-step method (Chorin 1968) alongside a second-order Adams–Bashforth scheme is used. Spatially, the equations

552

554

555

556

557

558

559

560

562

563

564

566

567

570

571

573

574

575

589

590

591

are discretized on a vertically staggered grid, where the horizontal derivatives are computed using discrete Fourier transforms, and the vertical derivatives are computed with second-order centred finite differences. The aliasing errors on the non-linear convective terms of the momentum and temperature equations are treated using the 3/2 rule (Canuto et al. 1988). Because of the spectral methods, the side boundary conditions are inherently periodic. The vertical velocity uses the non-penetration condition at the top and bottom of the domain, a stress-free lid condition is used as the top boundary conditions for the horizontal velocities, and a constant flux is imposed for the temperature top boundary condition. A wall model is used to prescribe the bottom wall-shear stress and surface flux through the vertical derivatives at the first staggered grid point (Moeng 1984; Bou-Zeid et al. 2004; Hultmark et al. 2013). This model uses Monin-Obukhov similarity theory to capture the effects of the thermal stratification on the ABL flow (Monin and Obukhov 1954) and applies Brutsaerts formulation of the atmospheric stability correction functions (Brutsaert 1982). Also, the scalar surface roughness length is set at one-tenth of the aerodynamic roughness length (Brutsaert et al. 1989). Note that although the stability correction functions were originally developed for flat homogeneous surfaces, these are used here because there is no better alternative, and this methodology has been shown to generate acceptable results over heterogeneous surface conditions as long as there exists a pseudo-equilibrium within the heterogeneities (Stoll and Porté-Agel 2008; Basu and Lacser 2017).

Finally, the numerical code is parallelized using a two-dimensional pencil decomposition where the domain is partitioned into squared cylinders (Sullivan and Patton 2011; Margairaz et al. 2018). The code uses the 2DECOMP & FFT open-source library to implement the two-dimensional pencil decomposition (Li and Laizet 2010). Further details on the numerical code used here can be found in Margairaz et al. (2018, 2020).

577 References

Albertson JD, Parlange MB (1999) Surface length scales and shear stress: Implications for land-atmospheric interaction over complex terrain. Water Resour Res 35(7):2121–2132

Basu S, Lacser A (2017) A cautionary note on the use of Monin-Obukhov
 similarity theory in very high-resolution large-eddy simulations. Boundary Layer Meteorol 163(2):351–355

Bejan A (2004) Convection Heat Transfer. Wiley

Bennett LJ, Weckwerth TM, Blyth AM, Geerts B, Miao Q, Richardson YP (2010) Observations of the evolution of the nocturnal and convective boundary layers and the structure of open-celled convection on 14 June 2002. Mon Weather Rev 138(7):2589–2607

Bou-Zeid E, Meneveau C, Parlange MB (2004) Large-eddy simulation of neutral atmospheric boundary layer flow over heterogeneous surfaces: Blending height and effective surface roughness. Water Resour Res 40(2):1–18

Bou-Zeid E, Meneveau C, Parlange MB (2005) A scale-dependent Lagrangian dynamic model for large eddy simulation of complex turbulent flows. Phys Fluids 17(2):025,105

- Brutsaert W (1982) Evaporation into the Atmosphere. Springer Netherlands,
 Dordrecht
- Brutsaert W, Parlange MB, Gash JHC (1989) Neutral humidity profiles in the
 boundary layer and regional evaporation from sparse pine forest. Annales
 Geophysicae 7:623–630
- Calaf M, Meneveau C, Parlange MB (2011) Large-eddy simulation study of a
 fully developed thermal wind-turbine array boundary layer. In: Kuerten H,
 Geurts B, Armenio V, Fröhlich J (eds) Direct and Large-Eddy Simulation
 VIII, ERCOFTAC Series, vol 15, Springer Netherlands, Dordrecht, pp 239–
- Canuto C, Hussaini MY, Quarteroni A, Zang TA (1988) Spectral Methods in
 Fluid Dynamics. Springer-Verlag, Berlin
- Chorin AJ (1968) Numerical solution of the Navier-Stokes equations. Mathematics of Computation 22:745–762
- Hultmark M, Calaf M, Parlange MB (2013) A new wall shear stress model for atmospheric boundary layer simulations. J Atmos Sci 70(11):3460–3470
 - Inagaki A, Letzel MO, Raasch S, Kanda M (2006) Impact of surface heterogeneity on energy imbalance: A study using LES. J Meteorol Soc Jpn 84(1):187–198

611

613

614

615

616

- Kanda M, Inagaki A, Letzel MO, Raasch S, Watanabe T (2004) LES study of the energy imbalance problem with eddy covariance fluxes. Boundary-Layer Meteorol 110(3):381–404
- Konrad TG (1970) The dynamics of the convective process in clear air as seen by radar. J Atmos Sci 27(8):1138–1147
 - Kravchenko AG, Moin P (1997) On the effect of numerical errors in large eddy
 simulations of turbulent flows. J Comput Phys 131(2):310-322
- Li N, Laizet S (2010) 2DECOMP & FFT A highly scalable 2D decomposition
 library and FFT interface. Cray User Group 2010 Conference pp 1–13
- Margairaz F, Giometto MG, Parlange MB, Calaf M (2018) Comparison of
 dealiasing schemes in large-eddy simulation of neutrally stratified atmospheric flows. Geosci Model Dev 11(10):4069–4084
- Margairaz F, Pardyjak E, Calaf M (2020) Surface thermal heterogeneities
 and the atmospheric boundary layer: The relevance of dispersive fluxes.
 Boundary-Layer Meteorol DOI 10.1007/s10546-020-00509-w
- Mauder M, Desjardins RL, Pattey E, Gao Z, van Haarlem R (2008) Measurement of the sensible eddy heat flux based on spatial averaging of continuous ground-based observations. Boundary-Layer Meteorol 128(1):151–172
- Moeng CH (1984) A large-eddy-simulation model for the study of planetary boundary-layer turbulence. J Atmos Sci 41(13):2052–2062
- Monin AS, Obukhov AM (1954) Basic laws of turbulent mixing in the surface layer of the atmosphere. Proceedings of Geophysics Institute, National Academy of Science, USSR 24(151):163–187

- Patton EG, Sullivan PP, Moeng CH (2005) The influence of idealized heterogeneity on wet and dry planetary boundary layers coupled to the land surface. J Atmos Sci 62(7):2078–2097
- Raupach MR, Shaw RH (1982) Averaging procedures for flow within vegetation canopies. Boundary-Layer Meteorol 22(1):79–90
- Salesky ST, Chamecki M, Bou-Zeid E (2017) On the nature of the transition between roll and cellular organization in the convective boundary layer. Boundary-Layer Meteorol 163(1):41–68
- Stoll R, Porté-Agel F (2008) Large-eddy simulation of the stable atmospheric
 boundary layer using dynamic models with different averaging schemes.
 Boundary-Layer Meteorol 126(1):1–28
- Stull RB (1988) An Introduction to Boundary Layer Meteorology. Springer Netherlands, Dordrecht
- Sullivan PP, Patton EG (2011) The effect of mesh resolution on convective
 boundary layer statistics and structures generated by large-eddy simulation.
 J Atmos Sci 68(10):2395–2415
- Tennekes H, Lumley JL (1972) A First Course in Turbulence, MIT Press
- Tritton DJ (1988) Physical Fluid Dynamics, second ed. Oxford University
 Press
- Weckwerth TM, Horst TW, Wilson JW (1999) An observational study of the
 evolution of horizontal convective rolls. Mon Weather Rev 127(9):2160–2179
- Zhou Y, Li D, Liu H, Li X (2018) Diurnal variations of the flux imbalance
 over homogeneous and heterogeneous landscapes. Boundary-Layer Meteorol
 168(3):417–442